PHYSICAL REVIEW B **96**, 125102 (2017)

# Experimental evidence for type-II Dirac semimetal in $PtSe_2$

Kenan Zhang,[1] Mingzhe Yan,[1] Haoxiong Zhang,[1] Huaqing Huang,[1] Masashi Arita,[2] Zhe Sun,[3]
Wenhui Duan,[1,4] Yang Wu,[5] and Shuyun Zhou[1,4,*]
[1]*State Key Laboratory of Low Dimensional Quantum Physics and Department of Physics, Tsinghua University, Beijing 100084, China*
[2]*Hiroshima Synchrotron Radiation Center, Hiroshima University, Higashihiroshima, Hiroshima 739-0046, Japan*
[3]*National Synchrotron Radiation Laboratory, University of Science and Technology of China, Hefei, Anhui 230029, China*
[4]*Collaborative Innovation Center of Quantum Matter, Beijing, China*
[5]*Department of Physics and Tsinghua-Foxconn Nanotechnology Research Center, Tsinghua University, Beijing 100084, China*
(Received 27 March 2017; published 1 September 2017)

While a monolayer $PtSe_2$ film is a semiconductor with interesting spin structure, bulk $PtSe_2$ crystal has been predicted to be a topological Dirac semimetal that can host a new type of Lorentz-violating Dirac fermions. Despite the intriguing predictions, experimental progress on the electronic structure of bulk $PtSe_2$ has been hindered due to the lack of large, high-quality single-crystal samples. Here we report the growth and characterization of high-quality $PtSe_2$ single crystals and reveal the electronic structure to provide direct evidence for the existence of three-dimensional type-II Dirac fermions. A comparison of the crystal, vibrational, and electronic structure to a related compound, $PtTe_2$, is also discussed. Our work provides an important platform for exploring the novel quantum phenomena associated with type-II Dirac fermions in the $1T$-$PtSe_2$ class of transition-metal dichalcogenides.

DOI: 10.1103/PhysRevB.96.125102

## I. INTRODUCTION

Dirac and Weyl fermions were originally introduced in high-energy physics [1]. Their counterparts in condensed-matter physics have been realized in three-dimensional (3D) Dirac and Weyl semimetals. Such topological semimetals exhibit a rich variety of novel phenomena, such as negative magnetoresistance (MR) [2–4], chiral magnetic effects [5], and the quantum anomalous Hall effect [6]. Dirac and Weyl semimetals can be classified into type I and type II, depending on whether the Lorentz invariance is preserved or not. For type-I Dirac [7,8] and Weyl semimetals [9–11], massless Dirac fermions with linear dispersions are expected at the Dirac or Weyl points. However, type-II Dirac and Weyl fermions [12] emerge at the topologically protected touching points of electron and hole pockets, and they show highly tilted Dirac cones along certain momentum directions [see schematics in Fig. 1(a)], thereby breaking the Lorentz invariance [13–15]. While type-I Dirac and Weyl semimetals exhibit negative MR along all directions, the MR properties of type-II semimetals are expected to be extremely anisotropic due to the anisotropic electronic structure, and negative MR is expected only along certain momentum directions where the cones are not tilted enough to break the Lorentz invariance [12,16,17]. A Dirac semimetal can be tuned to a Weyl semimetal or topological crystalline insulator when the crystal symmetry or time-reversal symmetry is broken [18,19], and therefore they are ideal candidates for investigating topological phase transitions and potential device applications.

Recently, the transition-metal dichalcogenide $PtTe_2$ with trigonal structure was reported to be a Lorentz-violating type-II Dirac semimetal [20]. $PtSe_2$ is isostructural to $PtTe_2$. Although a monolayer $PtSe_2$ film has been shown to exhibit interesting electronic properties [21] and helical spin texture with spin-layer locking [22,23] with intriguing applications in high-speed electronics [24–27] and spintronics, bulk $PtSe_2$ has been predicted to be a type-II Dirac semimetal [28]. So far experimental research in bulk $PtSe_2$ crystals has been limited due to the lack of high-quality single crystals. Here we report the growth and characterization of high-quality $PtSe_2$ single crystals and provide direct experimental evidence for type-II Dirac fermions from angle-resolved photoemission spectroscopy (ARPES). A comparison of $PtSe_2$ with $PtTe_2$ regarding crystal structure and vibrational and electronic structure is also presented.

## II. METHODS

Although high-quality $PtTe_2$ single crystals can be directly synthesized by a self-flux method as reported previously [20], such attempts to yield $PtSe_2$ have yet to be successful. Instead, we carried out chemical-vapor transport (CVT). The precursor of polycrystalline $PtSe_2$ was synthesized by directly heating the stoichiometric mixture of high-purity Pt granules (99.9%, Alfa Aesar) and a Se ingot (99.99%, Alfa Aesar) at 1173 K in a vacuum-sealed silica ampoule for 3 days. The polycrystalline $PtSe_2$ was then recrystallized by the CVT method using $SeBr_4$ (99%, Aladdin, with a concentration of $\leqslant 2.7$ mg/mL) as the transporting agent. The growth rate is much slower than $PtTe_2$. After 3 weeks, $PtSe_2$ single crystals a few millimeters in size with shiny surfaces were obtained.

The band structure calculations were carried out using density functional theory (DFT) implemented in the Vienna *Ab initio* Simulation Package (VASP) [29]. We employ the Perdew-Burke-Ernzerhof-type generalized gradient approximation [30] and the projector augmented-wave (PAW) method [31]. A plane-wave basis set with a default energy cutoff and an $18 \times 18 \times 11$ $k$-point mesh were used. Spin-orbit coupling is included self-consistently within the DFT calculation.

ARPES measurements were taken at BL13U at the Hefei National Synchrotron Radiation Laboratory, BL9A at the

---

[*] Corresponding author: syzhou@mail.tsinghua.edu.cn

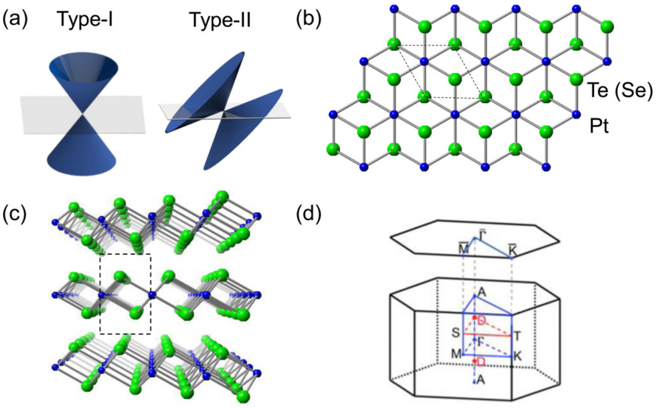

FIG. 1. Crystal structure and Brillouin zone of $PtSe_2$ ($PtTe_2$). (a) Schematic drawing of type-I and type-II Dirac fermions. (b) Top and (c) side views of the crystal structure of $PtSe_2$ ($PtTe_2$). Green balls are Se (Te) atoms, and blue balls are Pt atoms. The unit cell is indicated by black dashed lines. (d) BZ of bulk and the projected surface BZs of a (001) surface. The blue dots indicate the high-symmetry points of the BZ, and the red dots highlight the 3D Dirac point positions.

Hiroshima Synchrotron Radiation Center (under proposal number 15-A-26), and at our home laboratory. The crystals were cleaved *in situ* and measured at a temperature of $T \approx 20$ K in vacuum with a base pressure better than $1 \times 10^{-10}$ Torr. To determine the $PtSe_2$ $k_z$ dispersion, we use the free-electron final-state model $k_z = 0.512\sqrt{(h\nu - \Phi) \times \cos^2\theta + V_0}$, where $\Phi$ is the work function and $V_0$ is the inner potential [32]. We take an inner potential $V_0$ of 14 eV, which shows the best agreement between ARPES data and band structure calculations.

## III. RESULTS

Like its isostructural counterpart $PtTe_2$, $PtSe_2$ crystallizes in the centrosymmetric $CdI_2$-type structure with space group $P\bar{3}m1$ (No. 164) and point group $D_{3d}$ ($-3m$). The structure can be regarded as hexagonal close-packed Se atoms where Pt atoms occupy the octahedral sites in alternative Se layers. The adjacent unoccupied Se layers are held together by weak van der Waals interactions, which give rise the quasi-two-dimensional nature. The top and side views of the crystal structures of $PtSe_2$ ($PtTe_2$) are shown in Figs. 1(b) and 1(c). The hexagonal bulk and projected surface Brillouin zones (BZs) are shown in Fig. 1(d), where high-symmetry points and Dirac points are also indicated.

Figure 2 shows the characterization of the $PtSe_2$ single crystals compared to $PtTe_2$. Figures 2(a) and 2(b) show the x-ray diffraction (XRD) patterns, and only sharp (00l) diffraction peaks are observed. The larger diffraction angles for corresponding (00l) peaks of $PtSe_2$ compared to those of $PtTe_2$ suggest that $PtSe_2$ has a smaller layer separation. The extracted out-of-plane lattice constants are $c = 5.07 \pm 0.01$ Å for $PtSe_2$ and $c = 5.21 \pm 0.01$ Å for $PtTe_2$. The in-plane lattice constants are $a = b = 3.727$ Å for $PtSe_2$ and $a = b = 4.0242$ Å for $PtTe_2$ [33]. Figures 2(c) and 2(d) show the low-energy electron diffraction (LEED) pattern of the $PtSe_2$ and $PtTe_2$ single crystals after cleaving in an ultrahigh vacuum chamber. Sharp diffraction spots with hexagonal symmetry are observed on the entire sample surface, indicating the high-quality, homogeneous single crystals. Figures 2(e) and 2(f) show the temperature-dependent resistivity of $PtSe_2$ and $PtTe_2$ respectively. A metallic behavior is observed in both samples from 380 to 5 K with a high residual resistance ratio of 184 for $PtSe_2$ and 29 for $PtTe_2$. The large interlayer spacing of $PtSe_2$ leads to changes in the lattice vibrations. The Raman spectrum in Fig. 2(g) shows the $E_g$ and $A_{1g}$ modes at ~175 and 205 $\text{cm}^{-1}$, respectively, for $PtSe_2$, which are at much larger energies than those at 110 and 157 $\text{cm}^{-1}$ in $PtTe_2$ [Fig. 2(h)]. The $E_g$ mode involves the in-plane vibration with the top and the bottom Se atoms moving in opposite directions, and the $A_{1g}$ mode corresponds to the out-of-plane vibration of Se atoms. The blue shift of the Raman modes in $PtSe_2$ indicates a stronger interaction than $PtTe_2$ [34], which is in good agreement with the smaller layer separation.

The most important characteristic of a type-II Dirac semimetal is the tilted 3D Dirac cone in the band structure.

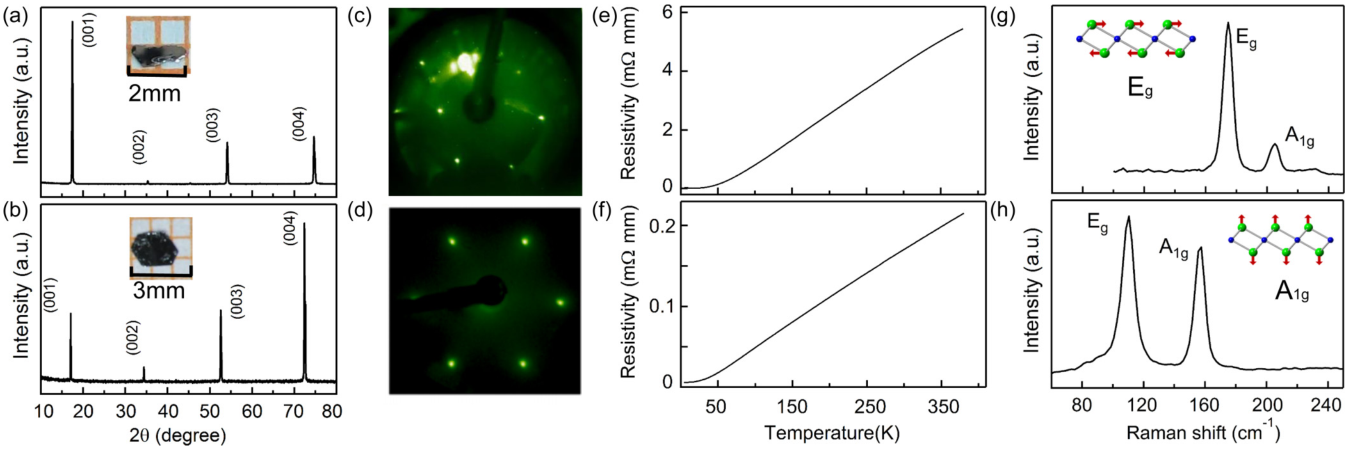

FIG. 2. Characterization of $PtSe_2$ compared to $PtTe_2$. X-ray diffraction patterns of (a) $PtSe_2$ and (b) $PtTe_2$ measured at room temperature. The inset shows a picture of the few-millimeter-size single crystal. LEED pattern of (c) $PtSe_2$ and (d) $PtTe_2$. Temperature-dependent resistivity of (e) $PtSe_2$ and (f) $PtTe_2$. Raman spectrum of (g) $PtSe_2$ and (h) $PtTe_2$ measured at room temperature. The inset illustrates vibrational modes in $PtSe_2$ or $PtTe_2$ with the same color code used in Fig. 1. Arrows guide the vibration directions.

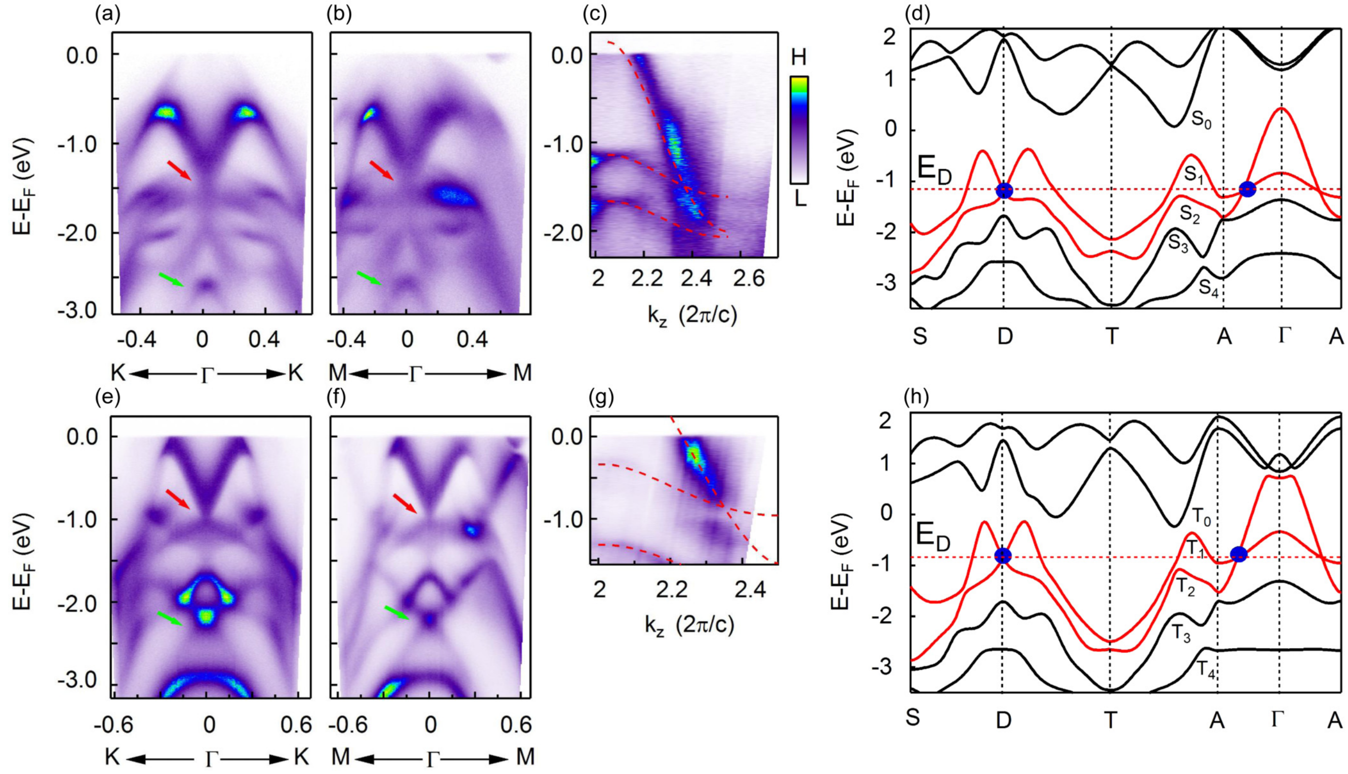

FIG. 3. Band structure of a type-II Dirac cone in PtSe$_2$ and PtTe$_2$. PtSe$_2$ band dispersions along the (a) Γ-*K* and (b) Γ-*M* directions at a photon energy of 23.5 eV ($k_z = 0.37c^*$). (c) $k_z$ dispersions of PtSe$_2$ measured at $k_\parallel = 0$. Red dashed lines are calculated dispersions for comparison. PtTe$_2$ band dispersions along the (e) Γ-*K* and (f) Γ-*M* directions at a photon energy of 22 eV ($k_z = 0.35c^*$). (g) $k_z$ dispersions of PtTe$_2$ measured at $k_\parallel = 0$. Calculated band dispersion of (d) PtSe$_2$ and (h) PtTe$_2$ along the in-plane direction *S*-*D*-*T* and out-of-plane direction *A*-Γ-*A* through the Dirac point *D*.

To reveal the 3D Dirac cone, we measure the dispersions around $k_\parallel = 0$ at different $k_z$ values using different photon energies. A conical dispersion is observed along the in-plane directions parallel to the Γ-*K* [Fig. 3(a)] and Γ-*M* [Fig. 3(b)] directions at $k_z = 0.37c^*$ ($c^* = 2\pi/c$) of the reduced BZ (All the $k_z$ data shown in this paper are in the second BZ). Along the out-of-plane direction [Fig. 3(c)], the dispersion shows a highly tilted Dirac cone crossing at the same $k_z$ value. The band dispersions of PtSe$_2$ are, overall, similar to those of PtTe$_2$ [Figs. 3(e)–3(h)] [20], except that the Dirac points are at slightly different energies ($-1.48$ compared to $-0.86$ eV) and at different $k_z$ values ($0.37c^*$ compared to $0.35c^*$). These differences are attributed to the different lattice constants. In addition, compared to PtTe$_2$, where the intensity is suppressed at the crossing point, PtSe$_2$ shows a 3D Dirac cone without any signature of suppression of intensity at the Dirac point. The suppression of intensity in PtTe$_2$ is likely induced by $k_z$ broadening, which is possibly weaker in PtSe$_2$ from the data. The anisotropic 3D Dirac cones that are highly tilted along the $k_z$ direction provide direct evidence of type-II Dirac fermions.

The type-II Dirac fermions in PtSe$_2$ are also supported by first-principles calculations and symmetry analysis. The 3D Dirac cone corresponds to the band crossing along the in-plane *S*-*D*-*T* momentum path in the calculated band structure in Fig. 3(d). The Dirac cone is strongly tilted along the Γ-*A* direction but not along the in-plane *S*-*D*-*T* path, which is the characteristic feature of the type-II Dirac fermions. The bulk Dirac cone of PtSe$_2$ is formed by two valence bands with Se *p* orbitals labeled as S$_1$ and S$_2$ in Fig. 3(d) (highlighted in red), while that of PtTe$_2$ is formed by two valence bands of Te *p* orbitals, labeled as T$_1$ and T$_2$ in Fig. 3(h). As each band is doubly degenerate, the isolated symmetry-protected band crossing is fourfold degenerate. Group-theory analysis shows that these two bands belong to different irreducible representations. More importantly, the $C_3$ rotational symmetry about the *c* axis prohibits hybridization between them and protects the 3D Dirac fermions. In addition to the 3D Dirac cone, there are also conical $Z_2$ surface states which are induced by the band inversion. The deep topological surface states are revealed in the ARPES data in Figs. 3(a) and 3(b) (indicated by green arrows), and they connect the gapped bulk bands S$_3$ and S$_4$ with opposite parities in Fig. 3(d). We perform a direct calculation of the $Z_2$ invariant using the Wannier charge-center methods and find $Z_2 = (1;000)$ for the subspace spanned by valence bands below the S$_3$ band. A comparison of dispersions along the $k_x$ direction at different $k_z$ values for PtSe$_2$, including the deep surface state which is independent of k$_z$, is shown in Figs. 4(a)–4(l). A similar type-II Dirac cone and deep topological surfaces also exist in PtTe$_2$ [Figs. 3(e)–3(g)].

Figure 5 shows a comparison of the electronic structures of PtSe$_2$ and PtTe$_2$ to reveal their difference. Figures 5(a)–5(e) and 5(h)–5(l) show the evolution of the constant-energy maps from $E_F$ to $-1.2$ eV. The Fermi surface map of PtSe$_2$ shows three small elliptical pockets around the Γ point [denoted as α

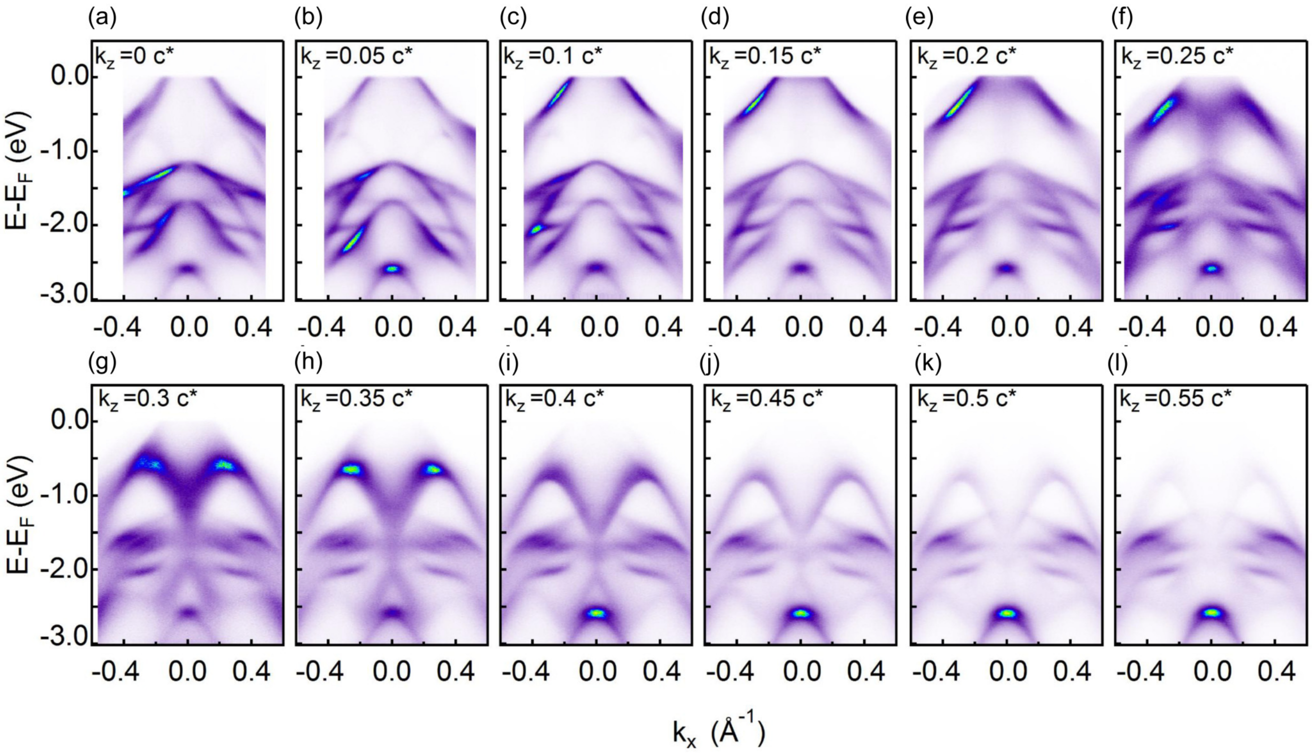

FIG. 4. (a)–(l) Comparison of linear dispersion in the $k_x$ direction at different $k_z$ for PtSe$_2$.

in Fig. 5(a)] and six pockets located at the midpoint between the Γ and $M$ points, which are from the bottom of the $\beta$ band [Fig. 5(g)]. Below $-0.4$ eV, there is an additional pocket emerging at the Γ point [Fig. 5(c)], and this pocket evolves into the 3D Dirac point at $k_z = 0.37c^*$ discussed above. The Fermi surface map of PtTe$_2$ features a small triangular pocket (denoted as $\gamma$) and six small circles (denoted as $\delta$) with alternating brightness located near the midpoint between Γ and $M$. The dispersions along the Γ-$K$ and Γ-$M$ directions are shown in Figs. 5(f) and 5(g) for PtSe$_2$ and in Figs. 5(m) and 5(n) for PtTe$_2$. The corresponding bands which contribute to $\alpha$, $\beta$ in Fig. 5(a) and $\gamma$, $\delta$ in Fig. 5(h) in the Fermi surface sheets are noted. The $\alpha$ and $\beta$ pockets in Fig. 5(g) are from the contributions of the S$_1$ and S$_0$ bands in Fig. 3(d), respectively. The $\gamma$ and $\delta$ pockets in Fig. 5(n) are from the contributions of the T$_1$ and T$_0$ bands in Fig. 3(h), respectively. A similar band structure can been found in PdTe$_2$ [35,36]. One major difference between the surface topologies of PtSe$_2$ and PtTe$_2$ is that the band at the midpoint between Γ and $M$ shows a gapped Dirac cone (indicated by the white arrow) in PtTe$_2$,

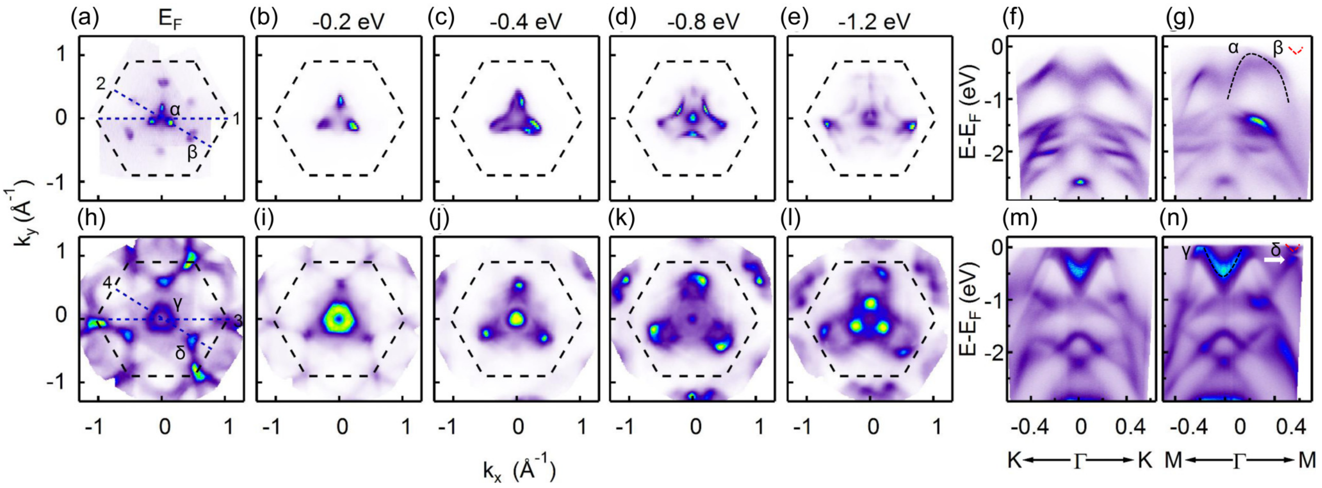

FIG. 5. Electronic structures of PtSe$_2$ and PtTe$_2$. (a)–(e) Intensity maps at constant energies from $E_F$ to $-1.2$ eV for PtSe$_2$ at a photon energy of 21 eV ($k_z = 0.29c^*$). The black dashed line indicates the surface BZ; the locations of two momentum cuts are marked by blue dashed lines. (f) and (g) High-symmetry direction cuts 1 and 2 in (a), respectively. (h)–(l) Intensity maps at constant energies from $E_F$ to $-1.2$ eV for PtTe$_2$ at a photon energy of 21.2 eV ($k_z = 0.3c^*$). The locations of two momentum cuts are marked by blue dashed lines. (m) and (n) High-symmetry direction cuts 3 and 4 in (h), respectively.

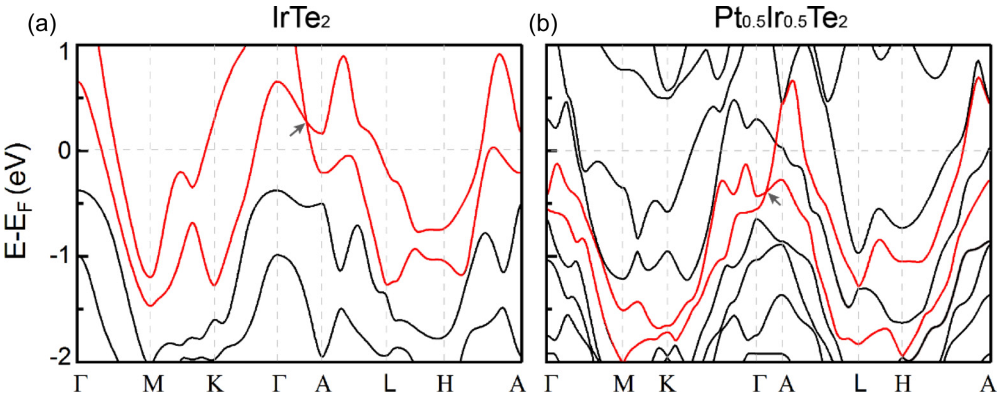

FIG. 6. Modulation of the electronic structures under chemical doping. (a) Calculated band dispersion of $IrTe_2$ along high-symmetry directions, resolving the tilted Dirac node above the Fermi level. (b) Calculated band dispersion of $Pt_{0.5}Ir_{0.5}Te_2$ along high-symmetry directions. The gray arrow indicates the tilted Dirac cone.

while there is only a small electron pocket in $PtSe_2$. The gapped Dirac cone is connected by the nontrivial surface states due to the extra band inversion for the top two bands at the Γ point in $PtTe_2$ [Fig. 3(h)]. Such a band inversion does not occur in $PtSe_2$, leading to different surface states.

The demonstration of Dirac fermions is an important step. However, the Dirac point energy is buried at ≈1 eV below $E_F$. Tuning the Dirac point to the Fermi energy is a critical step for further investigations of the transport properties. Element substitution and chemical doping have been widely used to tune the chemical potential. To induce holes in $PtSe_2$ and tune the chemical potential closer to the Dirac point, substitutions of Ir/Rh for Pt and As/Sb for Se are two possible solutions. We show preliminary calculations of the substitution for $PtTe_2$ in Fig. 6. Figure 6 shows that $IrTe_2$, which has the same crystal structure as $PtTe_2$ at room temperature, has a tilted Dirac node at 280 meV above the Fermi level, while the Dirac node in $Pt_{0.5}Ir_{0.5}Te_2$ is 390 meV below the Fermi level ($Pt_{0.5}Ir_{0.5}Te_2$). By fine-tuning the composition $x$, it is possible to tune the Dirac node energy of $Pt_{1-x}Ir_xTe_2$ to the Fermi energy. Such a $Pt_{1-x}Ir_xTe_2$ system is interesting for further investigation.

## IV. CONCLUSION

To summarize, by performing a systematic study of $PtSe_2$ single crystals, we provided experimental evidence for type-II Dirac fermions in $PtSe_2$. The differences in the lattice constant, vibrational modes, and electronic structure were also presented. Our work paves the way for studying a number of similar type-II Dirac materials in the $PtSe_2$ class of transition-metal dichalcogenides. This family of transition-metal dichalcogenides provides a platform for investigating novel electronic structures and topologic phase transition like the doping-driven Lifshitz transition [12,37] in the near future.

## ACKNOWLEDGMENTS

This work is supported by the National Natural Science Foundation of China (Grants No. 11427903 and No. 11334006) and the Ministry of Science and Technology of China (Grants No. 2015CB921001, No. 2016YFA0301001, and No. 2016YFA0301004).

---

[1] H. Weyl, Proc. Natl. Acad. Sci. USA **15**, 323 (1929).
[2] J. Xiong, S. K. Kushwaha, T. Liang, J. W. Krizan, M. Hirschberger, W. Wang, R. J. Cava, and N. P. Ong, Science **350**, 413 (2015).
[3] T. Liang, Q. Gibson, M. N. Ali, M. Liu, R. J. Cava, and N. P. Ong, Nat. Mater. **14**, 280 (2014).
[4] X. Huang, L. Zhao, Y. Long, P. Wang, D. Chen, Z. Yang, H. Liang, M. Xue, H. Weng, Z. Fang *et al.*, Phys. Rev. X **5**, 031023 (2015).
[5] A. A. Zyuzin and A. A. Burkov, Phys. Rev. B **86**, 115133 (2012).
[6] C. X. Liu, P. Ye, and X. L. Qi, Phys. Rev. B **87**, 235306 (2013); **92**, 119904(E) (2015).
[7] Z. K. Liu, B. Zhou, Y. Zhang, Z. J. Wang, H. M. Weng, D. Prabhakaran, S.-K. Mo, Z. X. Shen, Z. Fang, X. Dai, Z. Hussain, and Y. L. Chen, Science **343**, 864 (2014).
[8] M. Neupane, S.-Y. Xu, R. Sankar, N. Alidoust, G. Bian, C. Liu, I. Belopolski, T.-R. Chang, H.-T. Jeng, H. Lin, A. Bansil, F. Chou, and M. Z. Hasan, Nat. Commun. **5**, 3786 (2014).
[9] H. M. Weng, C. Fang, Z. Fang, B. A. Bernevig, and X. Dai, Phys. Rev. X **5**, 011029 (2015).
[10] B. Q. Lv, H. M. Weng, B. B. Fu, X. P. Wang, H. Miao, J. Ma, P. Richard, X. C. Huang, L. X. Zhao, G. F. Chen, Z. Fang, X. Dai, T. Qian, and H. Ding, Phys. Rev. X **5**, 031013 (2015).
[11] S.-Y. Xu, I. Belopolski, N. Alidoust, M. Neupane, G. Bian, C. Zhang, R. Sankar, G. Chang, Z. Yuan, C.-C. Lee, S.-M. Huang, H. Zheng, J. Ma, D. S. Sanchez, B. Wang, A. Bansil, F. Chou, P. P. Shibayev, H. Lin, S. Jia, and M. Z. Hasan, Science **349**, 613 (2015).
[12] A. A. Soluyanov, D. Gresch, Z. Wang, Q. Wu, M. Troyer, X. Dai, and B. A. Bernevig, Nature (London) **527**, 495 (2015).
[13] K. Deng, G. Wan, P. Deng, K. Zhang, S. Ding, E. Wang, M. Yan, H. Huang, H. Zhang, and Z. Xu, Nat. Phys. **12**, 1105 (2016).

[14] T.-R. Chang, S.-Y. Xu, G. Chang, C.-C. Lee, S.-M. Huang, B. Wang, G. Bian, H. Zheng, D. S. Sanchez, I. Belopolski *et al.*, Nat. Commun. **7**, 10639 (2016).

[15] L. Huang, T. M. McCormick, M. Ochi, Z. Zhao, M.-t. Suzuki, R. Arita, Y. Wu, D. Mou, H. Cao, J. Yan *et al.*, Nat. Mater. **15**, 1155 (2016).

[16] A. A. Zyuzin and R. P. Tiwari, JETP Lett. **103**, 717 (2016).

[17] F. Fei, X. Bo, R. Wang, B. Wu, J. Jiang, D. Fu, M. Gao, H. Zheng, Y. Chen, X. Wang, H. Bu, F. Song, X. Wan, B. Wang, and G. Wang, Phys. Rev. B **96**, 041201 (2017).

[18] A. A. Burkov and L. Balents, Phys. Rev. Lett. **107**, 127205 (2011).

[19] G. B. Halász and L. Balents, Phys. Rev. B **85**, 035103 (2012).

[20] M. Yan, H. Huang, K. Zhang, E. Wang, W. Yao, K. Deng, G. Wan, H. Zhang, M. Arita, H. Yang *et al.*, Nat. Commun. **8**, 257 (2017).

[21] Y. Wang, L. Li, W. Yao, S. Song, J. Sun, J. Pan, X. Ren, C. Li, E. Okunishi, Y.-Q. Wang *et al.*, Nano Lett. **15**, 4013 (2015).

[22] W. Yao, E. Wang, H. Huang, K. Deng, M. Yan, K. Zhang, K. Miyamoto, T. Okuda, L. Li, and Y. Wang, Nat. Commun. **8**, 14216 (2017).

[23] M. Yan, E. Wang, X. Zhou, G. Zhang, H. Zhang, K. Zhang, W. Yao, S. Yang, S. Wu, T. Yoshikawa *et al.*, arXiv:1703.04279.

[24] Y. Zhao, J. Qiao, Z. Yu, P. Yu, K. Xu, S. P. Lau, W. Zhou, Z. Liu, X. Wang, and W. Ji, Adv. Mater. **29**, 1604230 (2017).

[25] Z. Wang, Q. Li, F. Besenbacher, and M. Dong, Adv. Mater. **28**, 10224 (2016).

[26] C. Yim, K. Lee, N. McEvoy, M. O'Brien, S. Riazimehr, N. C. Berner, C. P. Cullen, J. Kotakoski, J. C. Meyer, and M. C. Lemme, ACS Nano **10**, 9550 (2016).

[27] X. Chia, A. Adriano, P. Lazar, Z. Sofer, J. Luxa, and M. Pumera, Adv. Funct. Mater. **26**, 4306 (2016).

[28] H. Huang, S. Zhou, and W. Duan, Phys. Rev. B **94**, 121117 (2016).

[29] G. Kresse and J. Furthmüller, Comput. Mater. Sci. **6**, 15 (1996).

[30] J. P. Perdew, K. Burke, and M. Ernzerhof, Phys. Rev. Lett. **77**, 3865 (1996).

[31] P. E. Blöchl, Phys. Rev. B **50**, 17953 (1994).

[32] A. Damascelli, Phys. Scr. **2004**, 61 (2004).

[33] G. Kliche, J. Solid State Chem. **56**, 26 (1985).

[34] M. O'Brien, N. McEvoy, C. Motta, J. Y. Zheng, N. C. Berner, J. Kotakoski, K. Elibol, T. J. Pennycook, J. C. Meyer, and C. Yim, 2D Mater. **3**, 021004 (2016).

[35] L. Yan, Z. Jian-Zhou, Y. Li, L. Cheng-Tian, H. Cheng, L. De-Fa, P. Ying-Ying, X. Zhuo-Jin, H. Jun-Feng, C. Chao-Yu *et al.*, Chin. Phys. B **24**, 067401 (2015).

[36] H. Noh, J. Jeong, E.-J. Cho, K. Kim, B. I. Min, and B.-G. Park, Phys. Rev. Lett. **119**, 016401 (2017).

[37] Y. Xu, F. Zhang, and C. Zhang, Phys. Rev. Lett. **115**, 265304 (2015).